Crystallite-growth, phase transition, magnetic properties, and sintering behaviour of nano-CuFe2O4 powders prepared by a combustion-like process

Roberto Köferstein, Till Walther, Dietrich Hesse, Stefan G Ebbinghaus

HAL Id: hal-01995690

https://hal.science/hal-01995690

Submitted on 27 Jan 2019

Crystallite growth, phase transition, magnetic properties, and sintering behaviour of nano-CuFe$_2$O$_4$ powders prepared by a combustion-like process

Roberto Köferstein[1)*], Till Walther[1)], Dietrich Hesse[2)] and Stefan G. Ebbinghaus[1)]

[1)] *Institute of Chemistry, Martin-Luther-University Halle-Wittenberg,*
Kurt-Mothes-Strasse 2, 06120 Halle, Germany.

[2)] *Max Planck Institute of Microstructure Physics, Weinberg 2, 06120 Halle, Germany.*

* Corresponding author. Tel.: +49-345-5525630; Fax: +49-345-5527028.
  E-mail address: roberto.koeferstein@chemie.uni-halle.de

Abstract. The synthesis of nano-crystalline CuFe$_2$O$_4$ powders by a combustion-like process is described herein. Phase formation and evolution of the crystallite size during the decomposition process of a (CuFe$_2$)-precursor gel were monitored up to 1000 °C. Phase-pure nano-sized CuFe$_2$O$_4$ powders were obtained after reaction at 750 °C for 2 h resulting in a crystallite size of 36 nm, which increases to 96 nm after calcining at 1000 °C. The activation energy of the crystallite growth process was calculated as 389 kJ mol^{-1}. The tetragonal $\leftrightarrows$ cubic phase transition occurs between 402 and 419 °C and the enthalpy change (ΔH) was found to range between 1020 and 1229 J mol^{-1} depending on the calcination temperature. The

optical band gap depends on the calcination temperature and was found between 2.03 and 1.89 eV. The shrinkage and sintering behaviour of compacted powders were examined. Dense ceramic bodies can be obtained either after conventional sintering at 950 °C or after a two-step sintering process at 800 °C. Magnetic measurements of both powders and corresponding ceramic bodies show that the saturation magnetization rises with increasing calcination-/ sintering temperature up to 49.1 emu g^{-1} (2.1 μ_B f.u.$^{-1}$), whereas the coercivity and remanence values decrease.

Keywords: *Copper ferrite; spinel; sintering; soft-chemistry synthesis, phase transition, magnetization*

1. Introduction

Copper ferrite ($CuFe_2O_4$) spinels are of interest because of their applications in advanced technologies [1]. *Traistaru* et al. [2] reported on the removal of nitrate from water using $CuFe_2O_4$ as a sorbent. Additionally, copper ferrite shows photocatalytic activity [3,4] and is also a candidate as catalyst for the partial reduction of methane [5] and in heterogeneous Fenton-like reactions for the wet peroxide oxidation of hydrocarbons [6]. Using $CuFe_2O_4$ as catalyst for the synthesis of medicinally important fluorinated spiropyrimidine derivatives has recently been reported by *Dandia* et al. [7]. Furthermore, copper ferrite can be applied as sensor material [8] and as anode material in lithium ion batteries [9,10]. *Yamashiro* [11] found electrical switching and memory effects in quenched $CuFe_2O_4$.

$CuFe_2O_4$ is ferrimagnetic with a *Curie* temperature around 500 °C [12,13]. At room temperature it crystallizes in the tetragonal spinel structure and transforms to a cubic one at about 400 °C [13]. The cubic cell parameter (SG: Fd$\bar{3}$m) is a = 837 pm [14]. The tetragonal unit cell of bulk $CuFe_2O_4$ (I4$_1$/amd, Z = 4) has parameters of a = 581 pm and c = 871 pm (c/a

= 1.50). This tetragonal unit cell can be transformed to a non-standard face-centred one (F4$_1$/ddm, Z = 8) with a´ = a·$\sqrt{2}$ and c´ = c (c/a´ = 1.06) [15,16,17]. Copper ferrite has a nearly complete inverse spinel structure and the Cu^{2+} distribution between the octahedral and tetrahedral sites depends on the heat treatment. The c/a ratio is influenced by the Cu^{2+} distribution [18].

Wet-chemical syntheses have been developed to obtain fine-grained and nano-sized $CuFe_2O_4$ powders [19,20,21,22]. A microwave assisted hydrothermal process was reported by *Thongtem* et al. [23].

The aim of this paper is to describe a facile and fast preparation route to obtain nano-sized $CuFe_2O_4$ powders in a combustion-like process. The formation of $CuFe_2O_4$ during the decomposition process was monitored by XRD and thermal analysis. Phase transition temperatures and enthalpy changes during transition from the tetragonal room-temperature to the cubic high-temperature modification were studied and the optical band gaps of the powders were calculated. The sintering behaviour and microstructure of resulting compacts were determined by dilatometry and SEM. Magnetic measurements were carried out both on $CuFe_2O_4$ powders and ceramic bodies.

2. Experimental

2.1. Material preparation

$Cu(CH_3COO)_2·H_2O$ (0.006 mol, *Merck*) and $Fe(NO_3)_3·9H_2O$ (0.012 mol, *Merck*) were dissolved in 15 ml water. Then, 3.15 g glycine (0.048 mol, *Merck*) and 2.88 g NH_4NO_3 (0.036 mol, *Fluka*) were added. After complete dissolving 2.00 g soluble starch (M = 324.30 g mol^{-1}, *Sigma-Aldrich*) was added. The turbid solution was continuously stirred at room temperature and after 15 min the temperature of the heating plate was raised to about 120 °C. After about 10 min the solution turned to a highly viscous black-brown gel. This (CuFe$_2$)-gel was calcined in static air at various temperatures from 300 °C to 1000 °C (heating rate 5 K min^{-1}, cooling

rate 10 K min^{-1}). The $CuFe_2O_4$, calcined at 700 °C for 10 h (powder **8**), was mixed with 5 wt.% of a saturated aqueous polyvinyl alcohol (PVA) solution as a pressing aid and then the powder was uniaxially pressed into pellets with a green density of about 2.1–2.2 g cm^{-3}.

2.2. Characterization

X-ray powder diffraction patterns were collected at room temperature on a *Bruker D8-Advanced* diffractometer, equipped with a one-dimensional silicon strip detector (LynxEye™) and operating with Cu-K$_\alpha$ radiation. The volume-weighted average crystallite sizes (column length) were determined from the XRD line broadening using the *Scherrer* equation [24] and the integral peak breadth. For that purpose the pseudo–Voigt function was used for profile fitting and the contribution of the strain-broadening was taken into account (software suite WinXPOW [25]). Dilatometric investigations were performed in flowing synthetic air (50 ml min^{-1}) in a *Setaram* TMA 92-16.18 dilatometer. Simultaneous thermogravimetric (TG) and differential thermoanalytic (DTA) measurements in flowing synthetic air (30 ml min^{-1}) were performed using a *Netzsch* STA 449 system. The TG/DTA measurements of the decomposition of the ($CuFe_2$)-gel were carried out on a sample preheated at 200 °C for 30 min. TEM images were recorded with a *Philips* CM20Twin at an electron energy of 200 keV. Scanning electron microscope images were recorded with a *Philips* XL30 ESEM (Environmental Scanning Electron Microscope). Magnetic measurements were carried out using a *Quantum Design* PPMS 9. Hysteresis loops were taken at 300 K and 10 K with magnetic field cycling between −90 and +90 kOe. Diffuse reflectance spectra were recorded at room temperature with a Perkin Elmer UV–Vis spectrometer Lambda 19. $BaSO_4$ was used as white standard.

3. Results and discussion

3.1. Powder characterization, TG-DTA, XRD and UV−Vis

Simultaneous TG/DTA investigations in air (heating rate 5 K min^{-1}) were carried out on a (CuFe$_2$)-gel preheated at 200 °C in air for 30 min (Fig. 1). A weight loss of 10.5 % up to 200 °C can be observed connected with a very weak exothermic signal. A following strong exothermic process with an onset temperature of 225 °C causes a total weight loss to 400 °C of 39.0 %. According to earlier investigations [26] the exothermic reaction suggests a self-combustion like process in which the nitrate ions act as an oxidizing agent and the (partly decomposed) starch and glycine molecules as well as the acetate ions as fuels. A following weight loss up to about 600 °C causes a total loss of 41.3 %. Further heating to 1000 °C reveals a very slight continuous weight loss resulting in a total weight loss of 42.5 %. XRD measurements of the black-brown reaction product reveal the formation of tetragonal CuFe$_2$O$_4$ [27].

Fig. 2 shows the phase evolution during the thermal decomposition of the black-brown (CuFe$_2$)-gel heated in a muffle furnace in static air at various temperatures for 2 h (heating rate 5 K min^{-1}, cooling rate 10 K min^{-1}). The starting (CuFe$_2$)-gel is X-ray amorphous (not shown). Calcination at 300 °C and 400 °C results in brown powders showing reflections of CuO and cubic CuFe$_2$O$_4$ [27] (Graph 2a). After heat treatment at 500 °C (Graph 2b) reflections of tetragonal CuFe$_2$O$_4$ along with CuO and Fe$_2$O$_3$ appear [27]. Calcination at 700 °C for 2 h (powder **1**) results in tetragonal CuFe$_2$O$_4$ with minor amounts of CuO and Fe$_2$O$_3$ (Graph 2c). Phase-pure dark-brown tetragonal CuFe$_2$O$_4$ (powder **2**) was obtained after calcination at 750 °C (Graph 2e). With increasing calcination temperature the colour gradually turns to black. The XRD pattern after calcination at 1000 °C (powder **7**, Graph 2f) for 1 h reveals the formation of very small traces of CuO, as seen in the magnification of the region 37° ≤ 2θ ≤ 43°. An explanation for the reappearance of CuO at high temperatures is given below. Prolonged calcination time up to 10 h at 700 °C also leads to phase-pure tetragonal CuFe$_2$O$_4$ (powder **8**, Graph 2d). In table 1 the calcination procedure, crystallite

sizes and cell parameters of selected samples are listed. As expected the crystallite size increases with calcination temperature. The c/a ratios of the powders **2–7** are almost constant. Analogous results were reported by *Iqbal* et al. [28]. TEM investigations (Fig. 3) of powder **8** show a main fraction of particles in the range between 42 and 110 nm, while larger particles up to 200 nm can only be found sporadically. The electron diffraction shown as inset is in accordance with the one calculated for the tetragonal spinel phase. The occurrence of sharp spots within the basically ring-shaped diffraction pattern indicates a high crystallinity of the sample.

Fig. 4 shows the evolution of the volume-weighted average crystallite size (*Scherrer* equation) depending on the calcination temperature of $CuFe_2O_4$. After a 2 h calcination procedure the crystallite sizes increase from 28 nm at 700 °C to 96 nm at 1000 °C (powder **1–7**).

The kinetics of crystallite growth can be expressed by the following phenomenological equation (1) [29]:

$$D^n - D_0{}^n = kt \cdot e^{\frac{-E_A}{RT}} \qquad (1)$$

where D_0 is the initial crystallite size, D the crystallite size after calcination for the time t and at temperature T, k is a pre-exponential constant, n the crystallite growth exponent, E_A the activation energy for the crystallite growth process and R the universal gas constant. The calculation of n is influenced by the value of the initial crystallite size (D_0). D_0 is usually negligibly small compared to D [30], so equation 1 can be simplified to:

$$D^n = kt \cdot e^{\frac{-E_A}{RT}} \qquad (2)$$

From the inverse slope of $\ln D$ vs. $\ln t$ the kinetic crystallite growth exponent n can be calculated. For this purpose the crystallite sizes were determined after calcining the ($CuFe_2$)-gel at 750 °C for different times from 2 h up to 100 h (Fig. 5a). The crystallite growth exponent was found to be $n = 9.7$. The activation energy of the crystallite growth process

6

during the calcination was calculated as $E_A = 389(17)$ kJ mol^{-1} from the slope of an Arrhenius plot of ln$D^{9.7}/t$ *versus* $1/T$ as shown in Fig. 5b.

DTA investigations up to 600 °C (10 K min^{-1}) on CuFe$_2$O$_4$ powders show both the tetragonal ⇄ cubic phase transition at ≈ 400 °C and the ferrimagnetic ⇄ paramagnetic transition (*Curie* temperature) at roughly 500 °C. Fig. 6 shows the DTA measurements for powders **2**, **5**, and **7**, exemplarily. The transition temperatures were determined by the onset of the DTA signal during the cooling phase [31]. The peak area of a DTA signal is proportional to the enthalpy change ΔH (Eq. 3) [32]:

$$\Delta H = k \cdot \frac{A}{m} \qquad (3)$$

where m is the sample mass, A the peak area and k is an instrument-specific factor. The DTA melting peak of zinc with $\Delta H = 7103.3$ J mol^{-1} (420 °C) [33] was used to determine the proportionality factor (k) assuming that its value does not significantly change in the studied temperature interval of the phase transitions of CuFe$_2$O$_4$.

Reported tetragonal ⇄ cubic phase transition temperatures are between 277 °C and 415 °C, while the *Curie* temperature is observed between 440 °C and 507 °C [12,13,18,22,28,34,35,36]. Our DTA measurements (Fig. 6) on CuFe$_2$O$_4$ powders calcined at 750 °C (**2**), 800 °C (**3**), 900 °C (**5**), 950 °C (**6**), and 1000 °C (**7**) (see also Tab. 1) reveal tetragonal ⇄ cubic phase transition temperatures of 419(1), 420(1), 408(1), 407(1), and 402(1) °C. The corresponding enthalpy changes were calculated as 1020(50), 1065(50), 1101(50), 1174(50) and 1229(50) J mol^{-1}, respectively. These phase transition enthalpies are in good agreement with the value of 1041 J mol^{-1} found by *Berbenni* et al. [13]. The investigations during the tetragonal ⇄ cubic phase transition show a small increase of the enthalpy change with rising crystallite sizes, which has also been observed in other systems as a typical size effect [37,38]. On the other hand the tetragonal ⇄ cubic phase transition temperature decreases with increasing crystallite sizes, i.e. increasing calcination temperature

(see inset in Fig. 6). As shown in Fig. 2 at a calcination temperature of 1000 °C weak reflections of CuO were detected, indicating that the resulting spinel phase has a copper deficit, as also observed by other authors [36,39]. In addition, during the calcination process a partial reduction of Cu^{2+} to Cu^+ in the spinel phase has been found [36,40,41]. The amount of Cu^+ depends on the calcination temperature and cooling procedure. Moreover, the formation of Fe^{2+} is also discussed [42,40]. *Brabers* and *Klerk* [36] observed small differences of the tetragonal $\leftrightarrows$ cubic phase transition temperature on samples with comparable c/a ratios. They pointed out that the above reduction process has an influence on the kinetic of the cation re-arrangement process, which influences the transition temperature.

The *Curie* temperature (ferrimagnetic $\leftrightarrows$ paramagnetic transition) does not significantly change with calcination temperature and was found to be 492(1) °C for powder **2** and 490(1) °C for powder **7**.

Fig. 7a shows the diffuse reflectance spectra of powders **2**, **3**, **4**, **5**, and **6** between 380 and 1000 nm. From the reflectance data the *Kubelka-Munk* function (F(R)) was calculated as described in an earlier paper [43]. Using the *McLean* analysis [44,45] the optical band gap can be described by a direct allowed transition according to *Selvan* at al. [46]. Thus, the optical band gap (E_g) can be determined by plotting $(F(R) \cdot h\nu)^2$ vs. $h\nu$ and extrapolating the slope to $F(R) \to 0$ (Fig. 7b). As seen in the inset of Fig. 7b, the optical band gap decreases with rising calcination temperature and is 2.03(1) eV (750 °C (**2**)), 2.02(1) eV (800 °C (**3**)), 1.94(2) eV (850 °C (**4**)), and 1.89(2) eV (900 °C (**5**)), respectively. Reported band gap values are in the range 1.42 to 3.09 eV [47,48]. From a calcination temperature of 950 °C the colour of the powders turns to black and the diffuse reflectance spectra show a nearly complete absorption of the light within the range from 380 to 1000 nm as can be seen for powder **6** (Fig. 7a).

3.2. Sintering behaviour and microstructure

Fig. 8a shows the non-isothermal dilatometric measurement up to 1100 °C in flowing air of compacts from powder **8**. A first weak shrinkage process starts at about 710 °C and at 870 °C the shrinkage increases considerably to a maximum value of −24.5 % at about 1040 °C. The shrinkage rate achieves a maximum at 913 °C with a value of −2.05 % min^{-1}, which indicates sliding processes as the dominant mechanism, because diffusion processes alone would result in shrinkage rates of less than −0.1 % min^{-1} [49,50]. Up to 1040 °C the non-isothermal shrinkage leads to a relative density of 90 %. Above ≈ 1050 °C a small expansion of the sintered body and thus a decrease in density can be observed. Reasons for the re-increasing $\Delta L/L_0$ above this temperature are discussed below.

The final bulk densities of ceramic bodies of powder **8** after isothermal conventional sintering (heating up with 10 K min^{-1}, soaking at this temperature for 1 h, and then cooling down with 10 K min^{-1}) at various temperatures in static air are shown in Fig. 8b. Microstructures of the selected sintered bodies are shown in Fig. 9. The absolute bulk densities of the sintered bodies were determined from their weight and geometric dimensions and the relative bulk densities were calculated with respect to the crystallographic density of 5.39 g cm^{-3} [53]. Sintering at 900 °C leads to ceramic bodies with a relative bulk density of 84 % and grain sizes between 0.35 and 2.9 µm as determined from the SEM images. The density rises to 96 % at 950 °C with grain sizes of 2.3−20 µm. However, higher sintering temperatures (1000 °C and 1100 °C) result in visibly porous bodies and in a corresponding reduction of the bulk densities to 91 % (grain sizes: 3.1−25 µm) and 64 % (grain sizes: 8.4−46 µm), respectively. Fig. 9a shows a heterogeneous grain-size distribution for conventional sintered ceramics. *Khedr* and *Farghali* [51] reported on $CuFe_2O_4$ ceramics synthesized from an acetate precursor, which reaches a relative density below 80 % after sintering at 1000 °C. As a result, the $CuFe_2O_4$ particles obtained from the decomposition of the starch/glycine precursor show improved sintering properties.

Both the isothermal sintering and the dilatometric investigation show that an expansion process starts at ≥ 1000 °C resulting in a decreasing density (Fig. 8). That effect is caused by the evaporation of gas, due to the thermal reduction of Cu^{2+}, which results in the formation of pores [52]. Fig. 10 shows the TG/DTA measurement (rate 10 K min^{-1}) of a ceramic body, sintered at 800 °C. The heating curve shows a very slight weight loss starting at about 900 °C, whereas a much more pronounced weight loss occurs above 1000 °C, connected with two broad endothermic signals at $T_{onset} = 968$ and 1044 °C. During the cooling process we observe an increase in weight below 980 °C. The observed weight loss during the heating process is due to the loss of oxygen and the partial reduction of Cu^{2+} to Cu^+ [36,39]. As seen, the re-oxidation during the cooling phase is not complete, because it is a slow process as described in [36,41]. *Parfenov* and *Nazipov* [40] found in $CuFe_2O_4$ samples sintered above 1000 °C and cooled to room temperature, that Cu^+ occupies the tetrahedral sites in the spinel structure. Furthermore, XRD investigations (not shown) on ceramic bodies sintered at 950 °C and 1100 °C for 1 h reveal tetragonal $CuFe_2O_4$ and small amounts of CuO, in contrast to ceramic bodies sintered at lower temperatures. As reported elsewhere [36,39,53], at high temperatures this partial reduction from Cu^{2+} to Cu^+ and the following re-oxidation lead to the segregation of CuO and a stable copper deficient ferrite. The reported formation of delafossite ($CuFeO_2$) at temperatures ≥ 1000 °C [54] was not observed in our measurements.

Using a two-step sintering procedure we obtained phase-pure dense ceramic bodies (rel. density ≥ 90 %) with small grain sizes even at lower sintering temperatures. For this purpose the compacts were first heated rapidly (30 K min^{-1}) to $T_1 = 950$ °C, then cooled (30 K min^{-1}) and held at a lower temperature (T_2). As seen in Fig. 8b, the two step sintering at $T_2 = 750$ °C and a soaking time of 5 h leads to ceramics with relative densities of 86 % and grain sizes in the range of 0.2−0.7 µm. Ceramic bodies with an even higher relative density of 92 % and grains between 0.3 and 1.6 µm can be obtained by increasing T_2 to 800 °C with a soaking

time of 2 h. Additionally, the ceramic bodies show a much more homogeneous grain size distribution compared to the conventional one-step sintering procedure, as a result of the suppressed grain-boundary migration during the two-step sintering procedure [55]. Table 2 summarizes the sintering results.

3.3. Magnetic measurements

The development of magnetization (M) depending on the applied field (H) at 300 K is demonstrated in Fig. 11a for powders **2**, **5** and **7**, calcined at 750 °C, 900 °C and 1000 °C, respectively. The saturation magnetization (M_s) was evaluated by linear extrapolation of the magnetization (high-field region) *versus* 1/H to 1/$H \rightarrow 0$, according to the *Law of Approach to Saturation* [56]. As shown in Fig. 12, rising calcination temperatures and thus larger crystallite sizes cause slightly increasing saturation magnetizations (M_s) (Fig. 12a), decreasing coercivities (H_c) (Fig. 12b) and remanences (M_r) (Fig. 12c). At 300 K we found M_s values between 24.5 and 26.5 emu g^{-1} (1.05 − 1.14 μ_B/mol), coercivities from 1.4 to 0.34 kOe, and remances between 12.1 and 8.7 emu g^{-1}. As expected, at 10 K the values rise to M_s = 27.5 − 29.8 emu g^{-1} (1.18 − 1.28 μ_B/mol), H_c = 1.6 − 0.36 kOe, and M_r = 14.4 − 9.9 emu g^{-1} (see Fig. 12a-c). The slight reduction of the saturation magnetization with decreasing crystallite size is due to the rising surface-to-volume ratio. Bulk $CuFe_2O_4$ has a collinear spin arrangement, whereas at the surface this spin orientation is disturbed resulting in a lower magnetization [57,58]. The reduced remanences (M_r/M_s) at 300 and 10 K for powders **2–5**, calcined between 750 and 900 °C, are between 0.46 and 0.52, which are very close to the theoretical value of 0.5 for non-interacting uniaxial single-domain particles [59]. On the other hand calcination at 1000 °C (powder **7**) results in a reduced remanence of 0.33 indicating a slightly increasing magnetostatic interaction [60].

M−H loops of ceramic bodies from powder **8** sintered between 800 and 1000 °C (Fig. 11b) show rising M_s values with increasing sintering temperatures up to 40.4 emu g^{-1} (1.73 μ_B/mol) at 300 K and 49.1 emu g^{-1} (2.10 μ_B/mol) at 10 K (Fig. 12d). The coercivities are between 1.4 − 0.053 kOe at 300 K and 1.6 − 0.155 kOe at 10 K (Fig. 12e). The fine-grained ceramic bodies from the two-step sintering process show an analogous behaviour with M_s values up to 31.4 emu g^{-1} (1.35 μ_B/mol) at 300 K and 36.4 emu g^{-1} (1.56 μ_B/mol) at 10 K (Fig. 12d). The dependence of M_s, H_c, and M_r on the sintering regime is shown in Fig. 12d-f and follows a similar trend as in the calcined powders. The higher M_s values of the ceramic bodies compared to the powder samples are due to the lower surface-to-volume ratio. Furthermore, the magnetization is also influenced by the distribution of Cu^{2+} between the octahedral and tetrahedral sites. Additionally, the large increase in magnetization above a sintering temperature of 900 °C is probably caused by the presence of diamagnetic Cu^+ on the tetrahedral site in the ceramic bodies. Moreover, *Thapa* et al. [42] reported on the formation of Fe^{2+}, which also causes an increase in magnetization.

Conclusion

Nano-crystalline $CuFe_2O_4$ powders were synthesized by a combustion-like reaction using starch and glycine as complexing agents and gellants. Phase-pure tetragonal $CuFe_2O_4$ was obtained after calcination of the resulting $(CuFe_2)$-gel at 750 °C for 2 h. The crystallite size of the powder reacted at 750 °C is 36 nm and grows to 96 nm after heating at 1000 °C. The activation energy for crystallite growth process was found to be 389(17) kJ mol^{-1}. The optical band gap varied between 2.03 and 1.89 eV depending on the calcination temperature. The enthalpy change during the tetragonal ⇆ cubic phase transition increases with increasing crystallite size, whereas the transition temperature decreases. During sintering of powder compacts of nano-sized $CuFe_2O_4$ the ceramic bodies reach relative densities up to 96 %.

Dense (rel. density $\geq 90\ \%$) and fine-grained ceramic bodies can also be obtained after a two-step sintering process at 800 °C. Sintering above 950 °C results in a decreasing density due to the reduction of Cu^{2+} to Cu^{+} and the evolution of oxygen. Magnetic measurements of both powders and ceramic bodies show that the saturation magnetization rises with increasing calcination-/ sintering temperature up to 49.1 emu g^{-1} (2.10 μ_B/mol), whereas the coercivity and remanence values decrease.

The $CuFe_2O_4$ powders show different magnetic properties depending on their particle sizes and heat treatment. This offers the possibility to modify magnetoelectric coupling phenomena in multiferroic composites. The improved sintering behaviour of the presented $CuFe_2O_4$ particles enables the fabrication of dense ceramic bodies at relatively low temperatures. With respect to multiferroic composites the synthesis approach in this work allows to obtain dense composite ceramic bodies with a lower risk of reaction between the components. Furthermore, the tuning of the optical band gap via the calcination temperature is of interest for photocatalytic applications.

Table 1

Crystallite sizes and lattice parameters

Powder	Calcination condition	d_{cryst} (nm)[1]	Cell parameter (pm)	c/a [2]
1	700 °C/ 2h	28		
2	750 °C/ 2h	36	a = 581.32, c = 871.76	1.500 (1.060)
3	800 °C/ 2h	46	a = 581.26, c = 871.97	1.500 (1.061)
4	850 °C/ 2h	58		
5	900 °C/ 2h	66	a = 581.36, c = 871.98	1.500 (1.061)
6	950 °C/ 2h	76		
7	1000 °C/ 2h	96	a = 581.63, c = 871.55	1.498 (1.059)
8	700 °C/ 10h	49		

1) volume-weighted average crystallite size (Scherrer equation)

2) numbers in brackets result from the non-standard setting (F4$_1$/ddm), a´ = a$\cdot \sqrt{2}$

Table 2

Sintering conditions, grain-sizes and relative densities of ceramic bodies
from powder **8**

Sintering procedure	Relative density (%)[a]	Grain-size range (µm)[b]
Conventional sintering (rate 10 K min^{-1})		
1000 °C/ 1h	91	3.0–37
950 °C/ 1h	96	2.3–20
900 °C/ 1h	84	0.35–2.9
800 °C/ 1h	52	0.15–0.6
Two-step sintering (rate 30 K min^{-1})		
T_1 = 950 °C, T_2 = 750 °C, 5h	86	0.2–0.7
T_1 = 950 °C, T_2 = 800 °C, 2h	91	0.3–1.6

a) the relative density is in relation to 5.39 g cm^{-3}
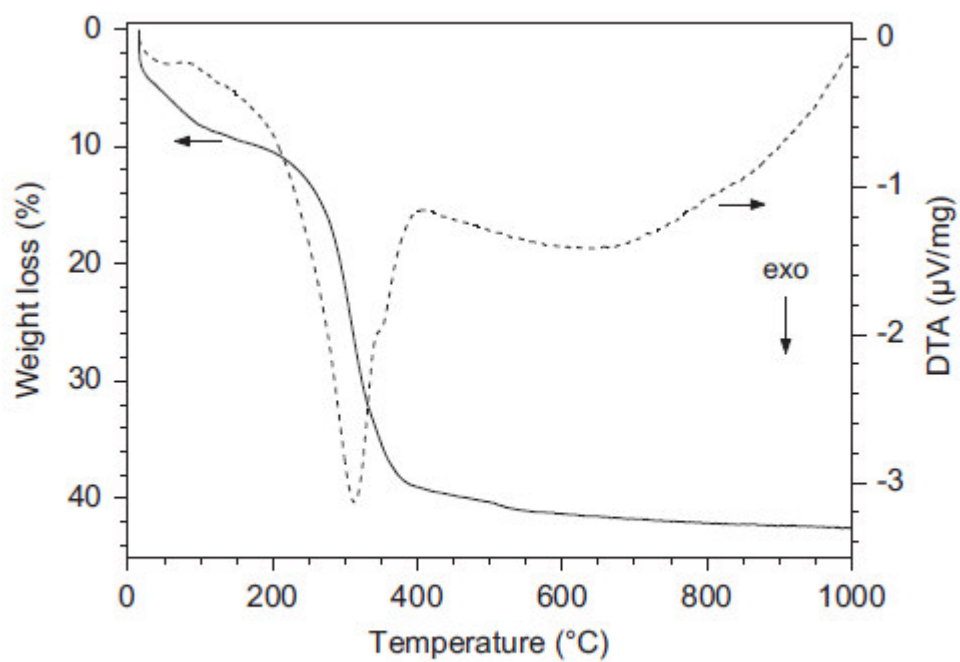b) determined from SEM images

Fig. 1. Simultaneous TG/DTA investigations of a preheated (CuFe$_2$)–gel in flowing air with a heating rate of 5 K min^{-1}.
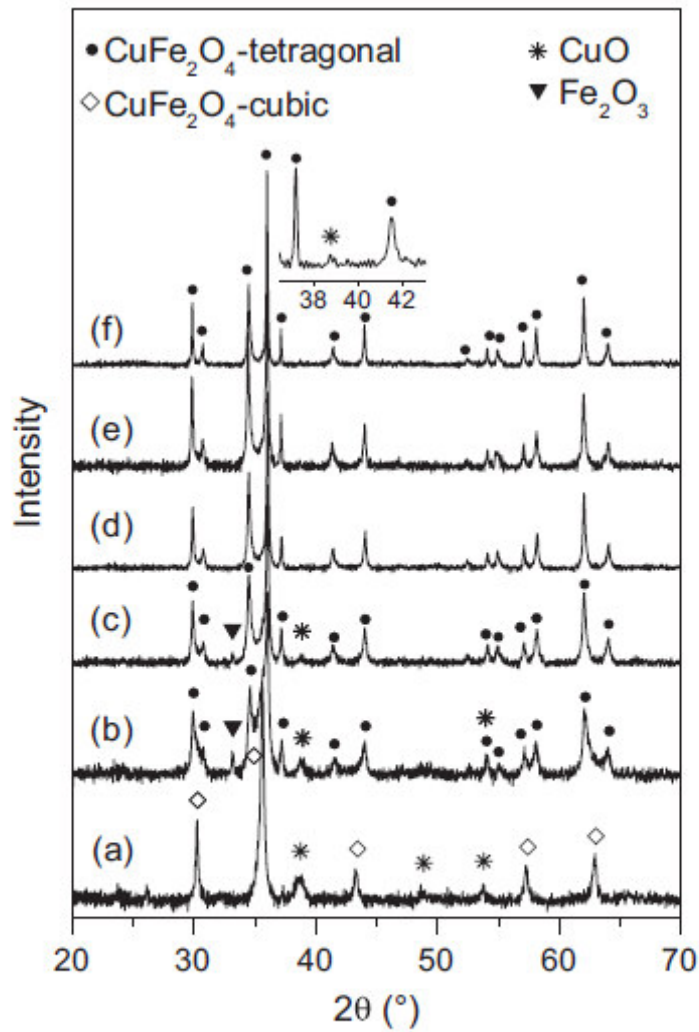
Fig. 2. Room temperature XRD patterns after calcination at various temperatures of the $(CuFe_2)$–gel (heating $5\,K\,min^{-1}$, cooling $10\,K\,min^{-1}$): (a) 300 °C, 2 h; (b) 500 °C, 2 h; (c) 700 °C, 2 h (powder **1**); (d) 700 °C, 10 h (powder **8**); (e) 750 °C, 2 h (powder **2**); (f) 1000 °C, 2 h (powder **7**).
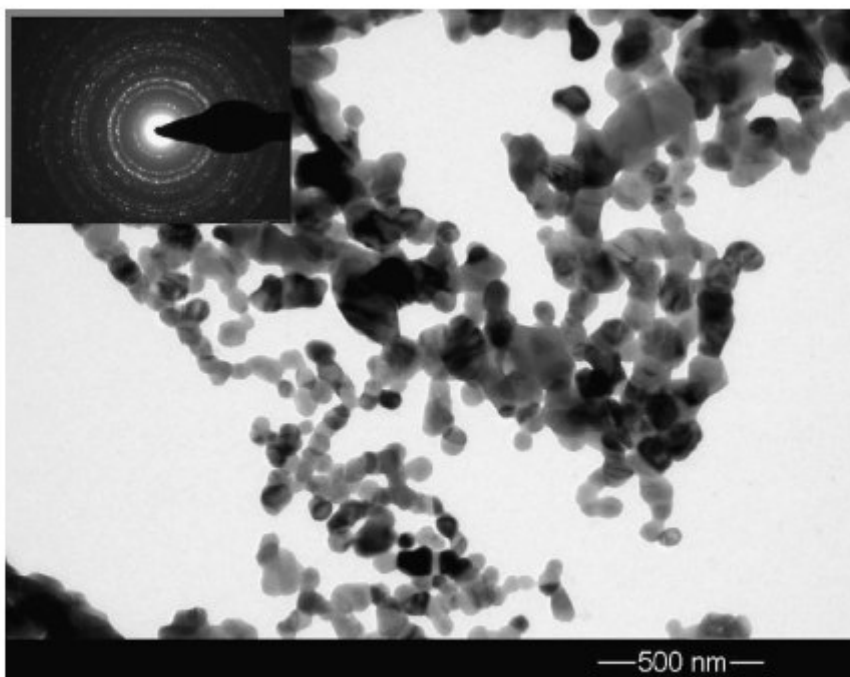
Fig. 3. TEM image of powder **8**. The inset shows the corresponding electron diffraction pattern.
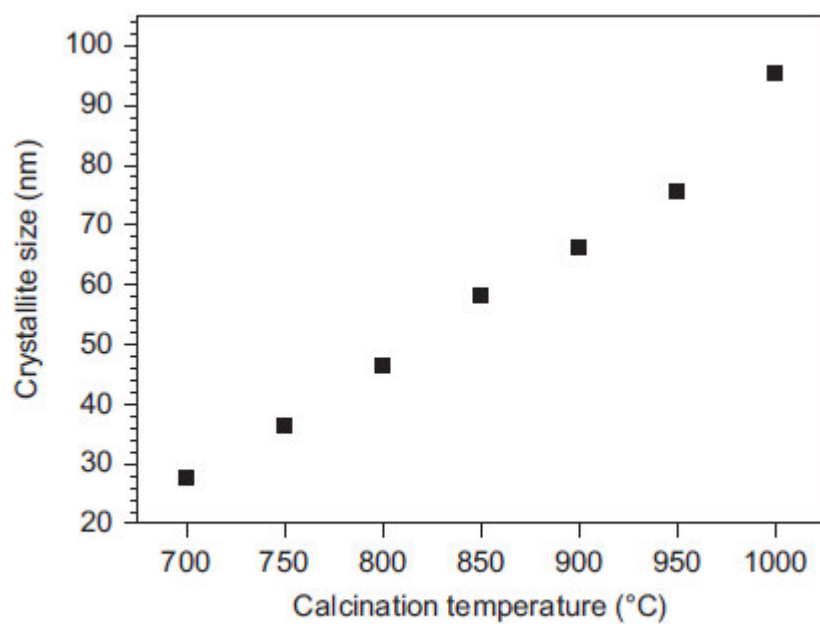
Fig. 4. Development of the volume-weighted average crystallite size with calcination temperature.
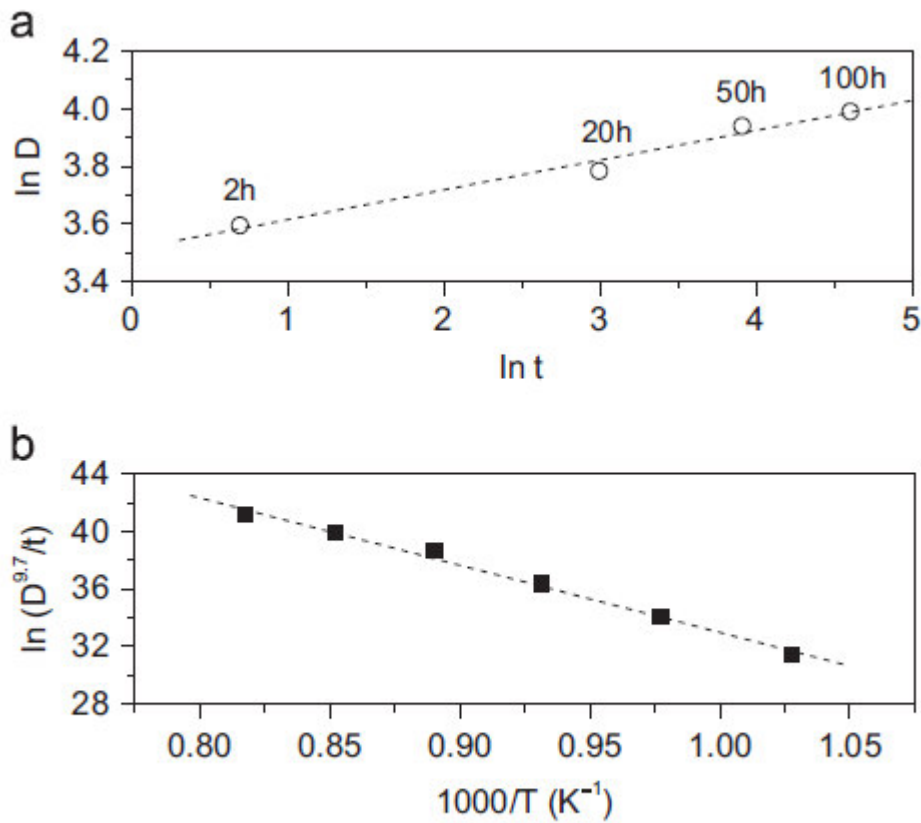
Fig. 5. (a) ln D (crystallite size) versus ln t (calcination time) for $CuFe_2O_4$ calcined at 750 °C. (b) Plot of ln $(D^{9.7}/t)$ as a function of $1/T$ at a calcination time of 2 h.
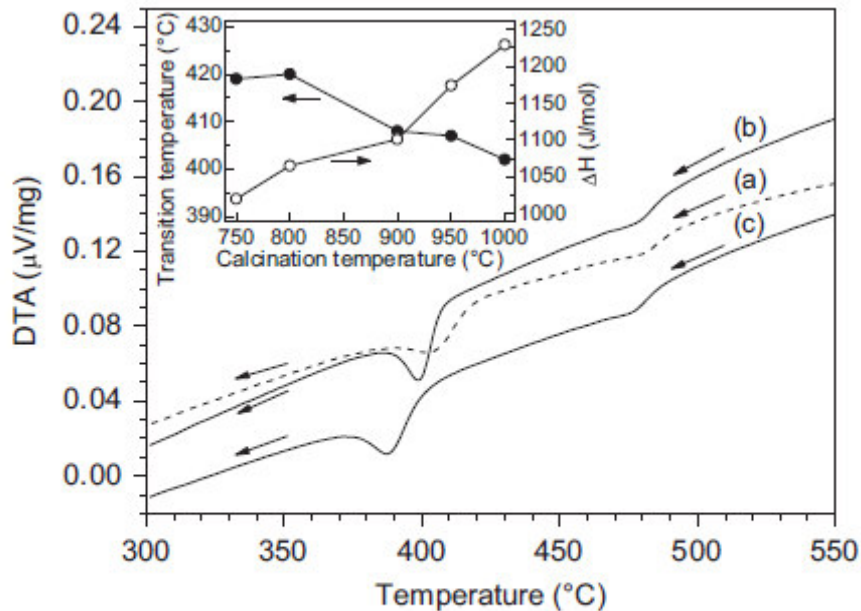

Fig. 6. DTA investigations in flowing air (rate 10 K min^{-1}) up to 600 °C of powders **2** (a), **5** (b), and **7** (c). The inset shows the transition temperature and the enthalpy change depending on the calcination temperature.
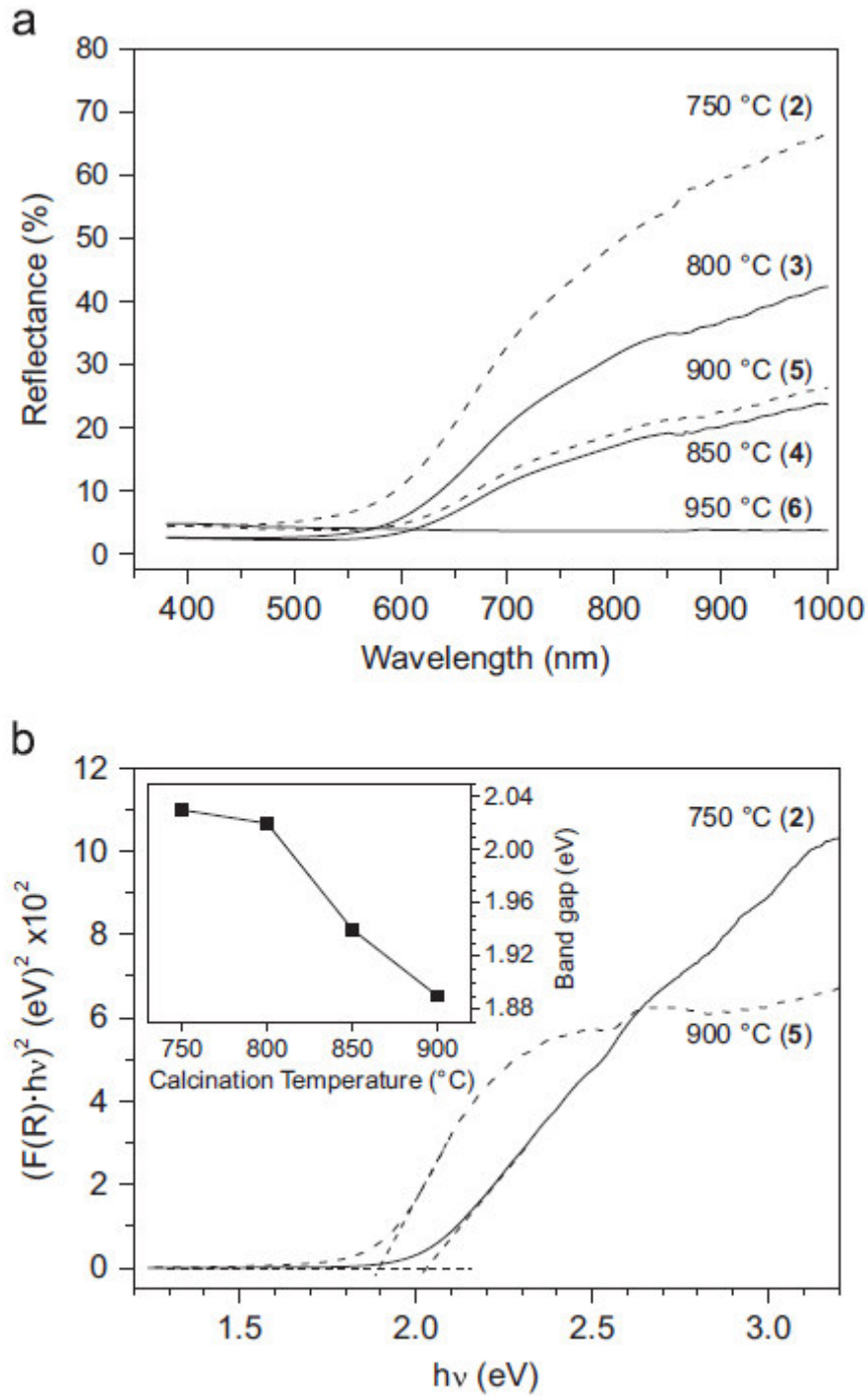
Fig. 7. (a) Diffuse reflectance spectra of selected powders. (b) Plot of $(F(R) \times h\nu)^2$ vs. $h\nu$ for powders **2** and **5**. The inset shows the optical band gap versus calcination temperature.
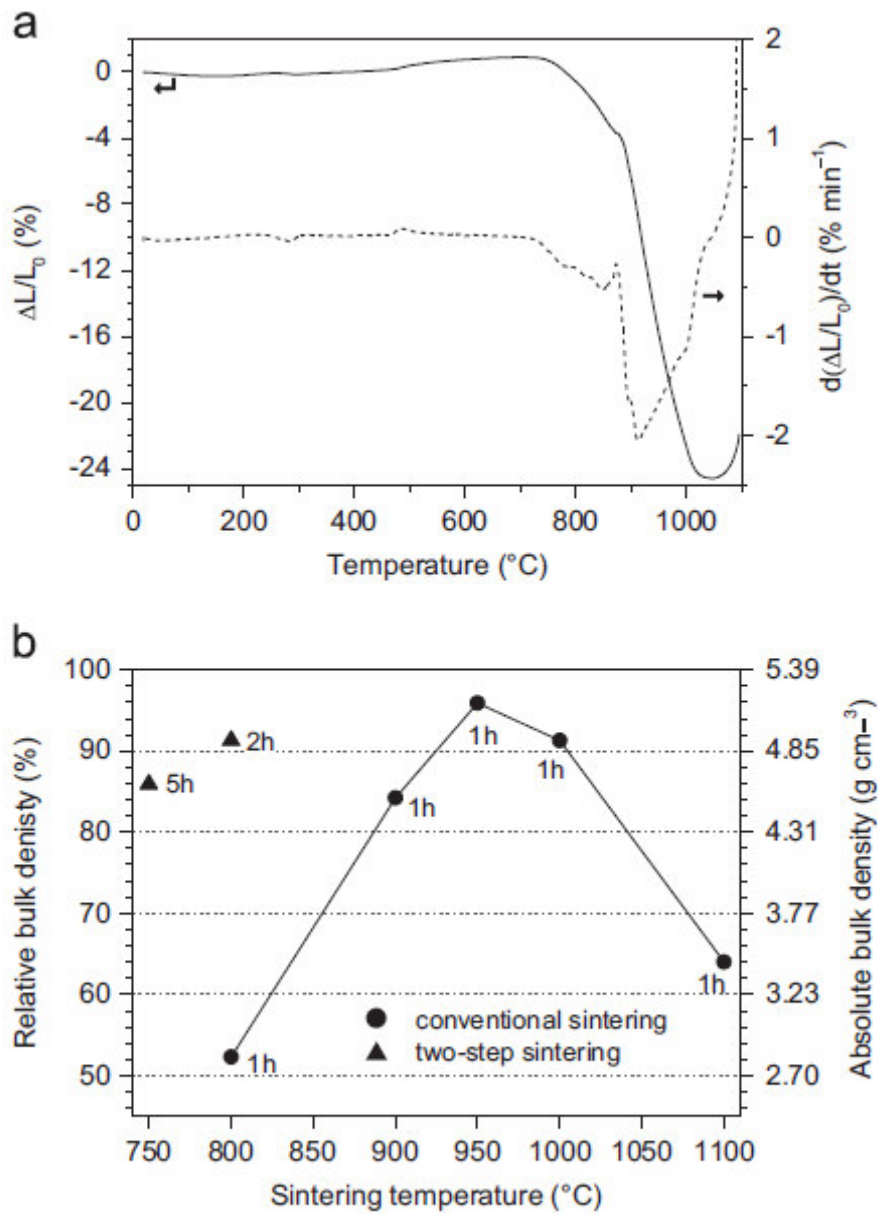
Fig. 8. (a) Non-isothermal dilatometric measurement of a green body of powder **8** in flowing air (heating rate 10 K min^{-1}). (b) Final bulk densities versus sintering temperature of ceramic bodies from powder **8** at the indicated soaking times.
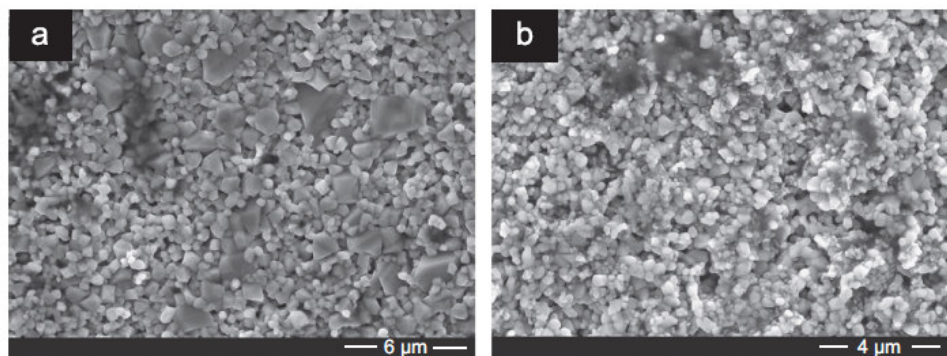

Fig. 9. SEM surface images of ceramic bodies of powder **8**. (a) conventional sintering at 900 °C, 1 h; (b) two-step sintering at $T_2=750$ °C, 5 h.
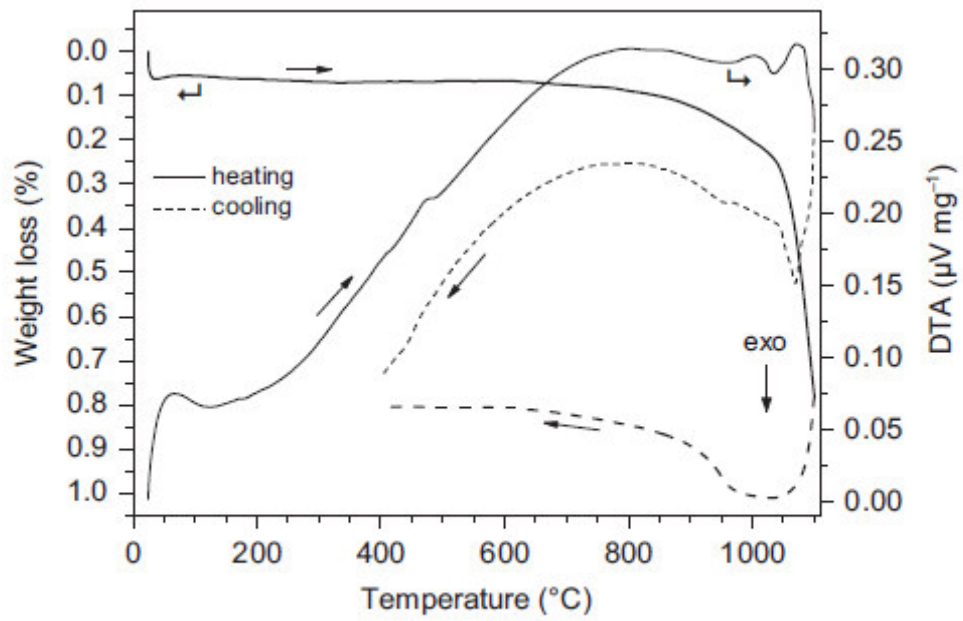
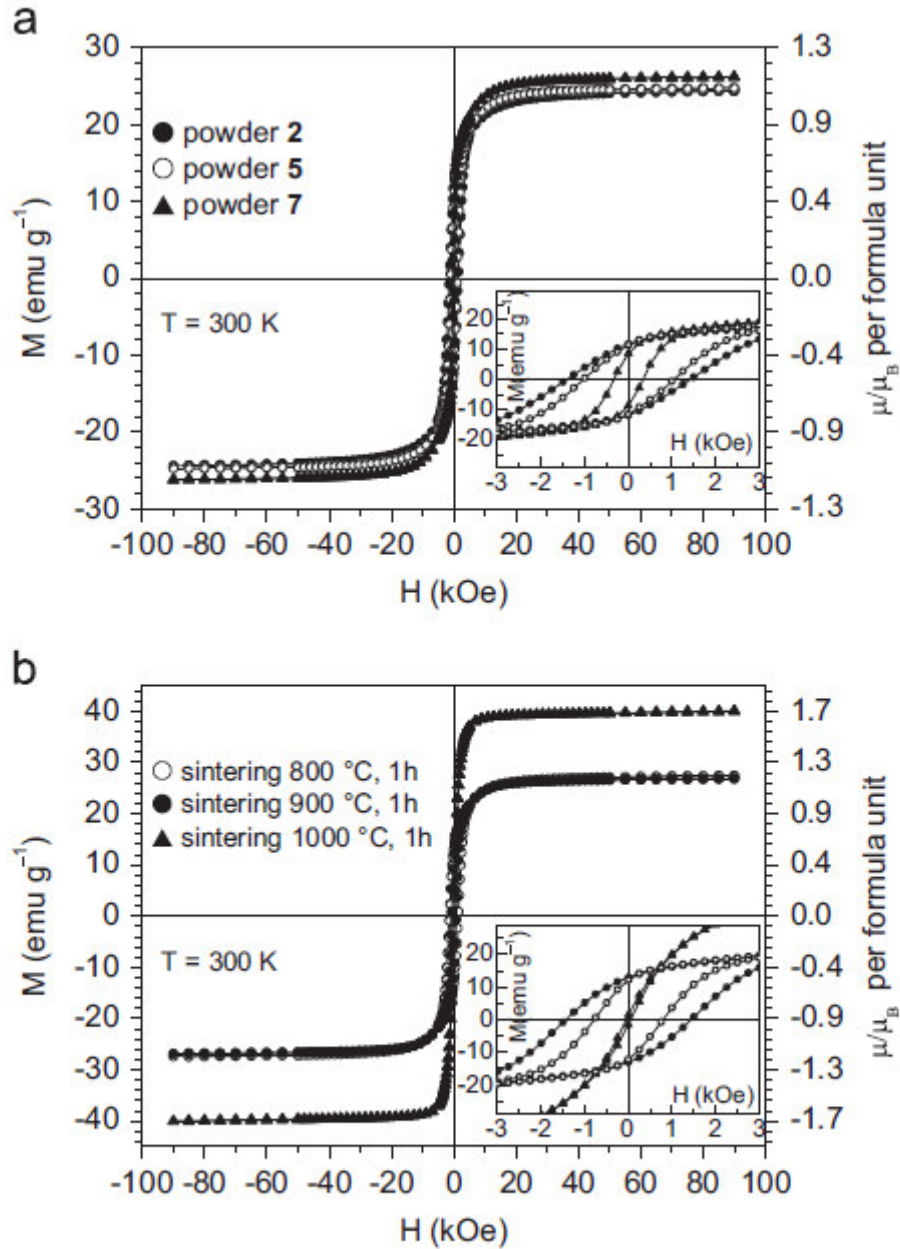**Fig. 10.** TG/DTA measurement of a ceramic body, sintered at 800 °C, with a heating-/cooling rate of 10 K min^{-1} in flowing air.

Fig. 11. Magnetization (M) versus applied magnetic field (H) at 300 K. (a) Powders after calcination at 750 °C (**2**), 900 °C (**5**), and 1000 °C (**7**). (b) Ceramic bodies from powder **8** after conventional sintering at 800, 900, and 1000 °C. The inset shows M versus H in a small field range.
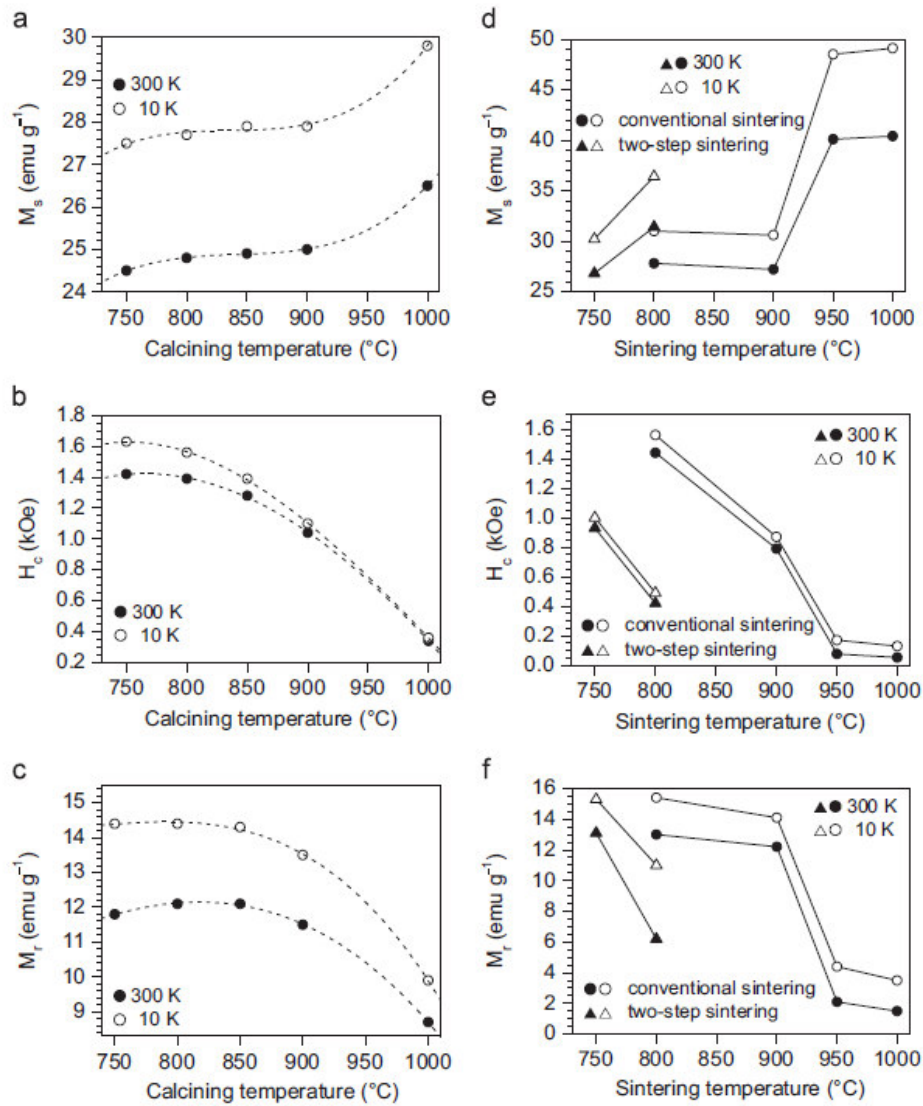
Fig. 12. Dependence of M_s, H_c, and M_r on the calcination (a, b, c) and sintering conditions (d, e, f), measured at 300 and 10 K. The lines are guides to the eyes.

References

[1] G.F. Goya, H.R. Rechenberg, J.Z. Jiang, *J. Appl. Phys.* 84 (1998) 1101–1108.

[2] G.A. Traistaru, C.I. Covaliu, G.P. Gallios, D.L. Cursaru, I. Jitaru, *Rev. Chim.* 63 (2012) 268–271.

[3] H. Yang, J. Yan, Z. Lu, X. Cheng, Y. Tang, *J. Alloys Compd.* 476 (2009) 715–719.

[4]   M.M. Rashad, R.M. Mohamed, M.A. Ibrahim, L.F.M. Ismail, E.A. Abdel-Aal, *Adv. Powder Technol.* 23 (2012) 315–323.

[5]   S.W. Woo, Y. Kang, K.S. Kang, C.H. Kim, C.S. Kim, C.S. Park, *Korean Chem. Eng. Res.* 46 (2008) 1113–1118.

[6]   H.-C. Lu, J.-E. Chang, W.-W. Vong, H.-T. Chen, Y.-L. Chen, *Int. J. Phys. Sci.* 6 (2011) 855–865.

[7]   A. Dandia, A.K. Jain, S. Sharma, *RSC Advances* 3 (2013) 2924–2934.

[8]   S. Singh, B.C. Yadav, V.D. Gupta, P.K. Dwivedi, *Mater. Res. Bull.* 47 (2012) 3538–3547.

[9]   M. Bomio, P. Lavela, J.L. Tirado, *J. Solid State Electrochem.* 12 (2008) 729–737.

[10]   Y. Ding, Y. Yang, H. Shao, *Solid State Ionics* 217 (2012) 27–33.

[11]   T. Yamashiro, *Japan J. Appl. Phys.* 12 (1973) 148–149.

[12]   B.J. Evans and S.S. Hafner, *J. Phys. Chem. Solids* 29 (1968) 1573–1588.

[13]   V. Berbenni, A. Marini, C. Milanese, G. Bruni, *J. Therm. Anal. Calorim.* 99 (2010) 437–442.

[14]   E.J.W. Verwey and E.L. Heilmann, *J. Chem. Phys.* 15 (1947) 174–180.

[15]   E. Prince and R.G. Treuting, *Acta Cryst.* 9 (1956) 1025–1028.

[16]   J. Darul, *Z. Kristallogr. Suppl.* 30 (2009) 335–340.

[17]   R.W.G. Wyckoff, *Crystal Structures* Vol. 3. John Wiley & Sons, Inc., New York, 1965.

[18]   X.-X. Tang, A. Manthiram, J.B. Goodenough, *J. Solid State Chem.* 79 (1989) 250–262.

[19]   C. Cannas, A. Falqui, A. Musinu, D. Peddis, G. Piccaluga, *J. Nanopart. Res.* 8 (2006) 255–267.

[20]   F. Kenfack, H. Langbein, *Thermochim Acta* 426 (2005) 61–72.

[21]   N.M. Deraz, *J. Alloys Compd.* 501 (2010) 317–325.

[22]   S. Manjura Hoque, S.S. Kader, D.P. Paul, D.K. Saha, H.N. Das, M.S. Rana, K. Chattopadhyay, M.A. Hakim, *IEEE Trans. Magn.* 48 (2012) 1839–1843.

[23]   T. Thongtem, A. Phuruangrat, S. Thongtem, *3rd IEEE International NanoElectronics Conference (INEC)* 1−2 (2010) 1070−1071.

[24]   Th.H. De Keilser, E.J. Mittermeijer, H.C.E Rozendaal, *J. Appl. Cryst.* 16 (1983) 309−316.

[25]   Program WinXPOW v1.06, Stoe & Cie GmbH, Darmstadt (1999).

[26]   R. Köferstein, S.G. Ebbinghaus, *Solid State Ionics* 231 (2013) 43–48.

[27]   PDF 2 (International Centre for Diffraction Data, Pennsylvania) 2001, $CuFe_2O_4$ [34-425]$_{tetragonal}$, $CuFe_2O_4$ [25-283]$_{cubic}$, CuO [48-1548], Fe_2O_3 [72-469].

[28]   M.J. Iqbal, N. Yaqub, B. Sepiol, B. Ismail, *Mater. Res. Bull.* 46 (2011) 1837–1842.

[29]   W. Cun, W. Xinming, Z. Jincai, M. Bixian, S. Guoying, P. Ping′an, F. Jiamo, *J. Mater. Sci.* 37 (2002) 2989−2996.

[30]   X.Y. Kang, T.D. Wang, Y. Han, M.D. Tao, M.J. Tu, *Mater. Res. Bull.* 32 (1997) 1165−1171.

[31]   H. K. Cammenga and M. Epple, *Angew. Chem.* 107 (1995) 1284−1301.

[32]   M.E. Brown, *Introduction to Thermal Analysis.* Chapman and Hall, New York, 1988.

[33]   S. Stølen and F. Grønvold, *Thermochim. Acta.* 327 (1999) 1−32.

[34]   D. Prabhu, A. Narayanasamy, K. Shinoda, B. Jeyadeven, J.-M. Greneche, K. Chattopadhyay, *J. Appl.Phys.* 109 (2011) 013532.

[35]   H.M. Zaki and S.F. Mansour, *Mater. Chem. Phys.* 88 (2004) 326–332.

[36]   V.A.M. Brabers and J. Klerk, *Thermochim. Acta* 18 (1977) 287–294.

[37]   R. Köferstein, L. Jäger, M. Zenkner, S.G. Ebbinghaus, *Mater. Chem. Phys.* 119 (2010) 118−122.

[38]   W.L. Zhong, B. Jiang, P. L. Zhang, J.M. Ma, H.M. Cheng, Z.H. Yang, L.X. Li, *J. Phys.: Condens. Mater.* 5 (1993) 2619–2624

[39]   F. Kenfack and H. Langbein, *Cryst. Res. Technol.* 39 (2004) 1070–1079.

[40]   V.V. Parfenov and R.A. Nazipov, *Inorg. Mater.* 38 (2002) 90–95.

[41]   E. Kordes and E. Röttig, *Z. Anorg. Allg. Chem.* 264 (1951) 34–47.

[42]   D. Thapa, N. Kulkarni, S.N. Mishra, P.L. Paulose, P. Ayyub, *J. Phys. D: Appl. Phys.* 43 (2010) 195004

[43]   R. Köferstein, T. Walther, D. Hesse, S.G. Ebbinghaus, J. *Mater. Sci.* 48 (2013) 6509–6518.

[44]   M. Nowak, B. Kauch, P. Szperlich, *Rev. Sci. Instrum.* 80 (2009) 046107.

[45]   T.P McLean, in: Progress in Semiconductors, ed. A.F. Gibson, Heywood, London, 1960, Vol. 5, pp. 55−102.

[46]   R.K. Selvan, V. Krishnan, C.O. Augustin, H. Bertagnolli, C.S. Kim, A. Gedanken, *Chem. Mater.* 20 (2008) 429–439.

[47]   A. Kezzim, N. Nasrallah, A. Abdi, M. Trari, *Energ. Convers. Manage.* 52 (2011) 2800–2806.

[48]   S. Singha, B.C. Yadava, R. Prakashb, B. Bajajc, J. Rock lee, *Appl. Surf. Sci.* 257 (2011) 10763– 10770.

[49]   R. Köferstein, L. Jäger, M. Zenkner, S.G. Ebbinghaus, *J. Eur. Ceram. Soc.* 29 (2009) 2317−2324.

[50]   W. Schatt, *Sintervorgänge.* VDI-Verlag, Düsseldorf, 1992, pp. 78–100.

[51]   M.H. Khedr and A.A. Farghali , *J. Mater. Sci. Technol.* 21 (2005) 675–680.

[52]   S. Akhter, D.P. Paul, M.A. Hakim, S. Akhter, D.K. Saha, B. Anjuman, F. Islam, *J. Sci. Res.* 4 (2012) 551–560.

[53]   P.L. Weil, F. Bertaut, L. Bochirol, *J. Phys. Rad.* 11 (1950) 208–212.

[54] N.-H. Li, S.-L. Lo, C.-Y. Hu, C.-H. Hsieh, C.-L. Chen, *J. Hard. Mater.* 190 (2011) 597–603.

[55] X.-H. Wang, X.-Y. Deng, H. Zhou, L.-T. Li, I.-W. Chen, *J. Electroceram.* 21 (2008) 230–233.

[56] S. Chikazumi (2005) Physics of Ferromagnetism. Oxford University Press.

[57] J. Janicki, J. Pietrzak, A. Porebska, J. Suwalski, *phys. stat. sol.* 72 (1982) 95–98.

[58] K. Haneda and A.H. Morrish, *J. Appl. Phys.* 63 (1988) 4258–4260.

[59] L.D. Tung, V. Kolesnichenko, D. Caruntu, N.H. Chou, C.J. O'Connor, L. Spinu, *J. Appl. Phys.* 93 (2003) 7486–7488.

[60] M. Gharagozlou, *J. Alloys Compd.* 486 (2009) 660–665.